The microcircuits of striatum in silico

J. J. Johannes Hjorth[a,1], Alexander Kozlov[a,b,1], Ilaria Carannante[a,2], Johanna Frost Nylén[b,2], Robert Lindroos[b,2], Yvonne Johansson[b,3], Anna Tokarska[b,3], Matthijs C. Dorst[b,3], Shreyas M. Suryanarayana[b], Gilad Silberberg[b], Jeanette Hellgren Kotaleski[a,b,4,5], and Sten Grillner[b,4,5]

[a]Science for Life Laboratory, School of Electrical Engeneering and Computer Science, Royal Institute of Technology, SE-10044 Stockholm, Sweden; and [b]Department of Neuroscience, Karolinska Institutet, SE-17165 Stockholm

Contributed by Sten Grillner, March 6, 2020 (sent for review January 14, 2020; reviewed by Rui Costa and Sean Hill)

The basal ganglia play an important role in decision making and selection of action primarily based on input from cortex, thalamus, and the dopamine system. Their main input structure, striatum, is central to this process. It consists of two types of projection neurons, together representing 95% of the neurons, and 5% of interneurons, among which are the cholinergic, fast-spiking, and low threshold-spiking subtypes. The membrane properties, soma–dendritic shape, and intrastriatal and extrastriatal synaptic interactions of these neurons are quite well described in the mouse, and therefore they can be simulated in sufficient detail to capture their intrinsic properties, as well as the connectivity. We focus on simulation at the striatal cellular/microcircuit level, in which the molecular/subcellular and systems levels meet. We present a nearly full-scale model of the mouse striatum using available data on synaptic connectivity, cellular morphology, and electrophysiological properties to create a microcircuit mimicking the real network. A striatal volume is populated with reconstructed neuronal morphologies with appropriate cell densities, and then we connect neurons together based on appositions between neurites as possible synapses and constrain them further with available connectivity data. Moreover, we simulate a subset of the striatum involving 10,000 neurons, with input from cortex, thalamus, and the dopamine system, as a proof of principle. Simulation at this biological scale should serve as an invaluable tool to understand the mode of operation of this complex structure. This platform will be updated with new data and expanded to simulate the entire striatum.

modeling | basal ganglia | network | compartmental models | computational analysis

One important role of the brain is to help the organism make appropriate decisions adapted to the needs of a given situation and implement these decisions as well-coordinated actions appropriate to the conditions. This could relate to anything from escape or aggressive behavior to more subtle actions like eye movement or playing the piano. The basal ganglia play a major role in this context together with their input from the cortex, thalamus, and the dopamine system. In rodents the dorsolateral part of the striatum, the extensive basal ganglia input stage, is involved in the control of innate movements and the learned motor patterns referred to as habits (1–3), whereas the dorsomedial part is thought to be involved in goal-directed movements, that is, novel movements adapted to a given situation. The difference between the two types of movements is not distinct. One may envision the relative roles of the cortex and striatum in that cortex broadcasts a wish to generate a given movement, whereas striatum would actually decide whether it will be implemented or not (4). Our aim here is to simulate the microcircuits of striatum, based on detailed information on cellular properties of striatal projection neurons and interneurons and their connectivity within striatum, and partially on data from experiments performed within this study.

The striatum (Fig. 1*A*) is by far the largest and most complex part of the basal ganglia (5). Additional components of the basal ganglia are their output nuclei, the substantia nigra pars reticulata (SNr) and globus pallidus interna (GPi, in rodents also named entopeduncular nucleus), and the intrinsic nuclei, the subthalamic nucleus (STN) and globus pallidus externa (GPe, in rodents also GP). The mouse striatum consists of around 1.7 million neurons, whereas the output nuclei are much smaller, each having less than 2% of the number of neurons in striatum.

Striatum integrates information from different parts of the cortex, thalamus, pedunculopontine nucleus (PPN) and the dopamine system (substantia nigra pars compacta [SNc] and ventral tegmental area). In the rodent striatum, 95 to 96% of the neurons are GABAergic striatal projection neurons (SPN) that are divided into two subpopulations, one that expresses the dopamine 1 receptor (D1R) and substance P (SP) and targets directly the output nuclei (GPi/SNr), representing the "direct pathway" (Fig. 1*B1*), which can initiate movements through disinhibition of brainstem motor centers. They are therefore called dSPNs. The

Significance

Our aim is to reconstruct a full-scale mouse striatal cellular level model to provide a framework to integrate and interpret striatal data. We represent the main striatal neuronal subtypes, the two types of projection neurons (dSPNs and iSPNs) giving rise to the direct and indirect pathways, the fast-spiking interneurons, the low threshold spiking interneurons, and the cholinergic interneurons as detailed compartmental models, with properties close to their biological counterparts. Both intrastriatal and afferent synaptic inputs (cortex, thalamus, dopamine system) are optimized against existing data, including short-term plasticity. This model platform will be used to generate new hypotheses on striatal function or network dynamic phenomena.

Author contributions: J.J.J.H., A.K., J.H.K., and S.G. designed research; J.J.J.H., A.K., I.C., J.F.N., R.L., Y.J., A.T., M.C.D., J.H.K., and S.G. performed research; J.J.J.H., A.K., I.C., J.F.N., R.L., J.H.K., and S.G. contributed new reagents/analytic tools; J.J.J.H., A.K., I.C., J.F.N., R.L., Y.J., A.T., M.C.D., S.M.S., G.S., J.H.K., and S.G. analyzed data; J.J.J.H., A.K., S.M.S., J.H.K., and S.G. wrote the paper; and G.S. supervised the entire experimental analysis.

Reviewers: R.C., Columbia University; and S.H., University of Toronto.

The authors declare no competing interest.

Data deposition: The striatal model is hosted in EBRAINS (https://kg.ebrains.eu/search/instances/Model/a6458de3-a176-4378-9b03-34a26f5da3bd). The code is publicly available on GitHub (https://github.com/Hjorthmedh/Snudda/), and through the Human Brain Project platform (detailed information about modeling and experiments is included in *SI Appendix*).

[1]J.J.J.H. and A.K. contributed equally to this work.

[2]I.C., J.F.N., and R.L. contributed equally to this work.

[3]Y.J., A.T., and M.C.D. contributed equally to this work.

[4]J.H.K. and S.G. contributed equally to this work.

[5]To whom correspondence may be addressed. Email: jeanette@kth.se or sten.grillner@ki.se.

This article contains supporting information online at https://www.pnas.org/lookup/suppl/doi:10.1073/pnas.2000671117/-/DCSupplemental.

First published April 22, 2020.

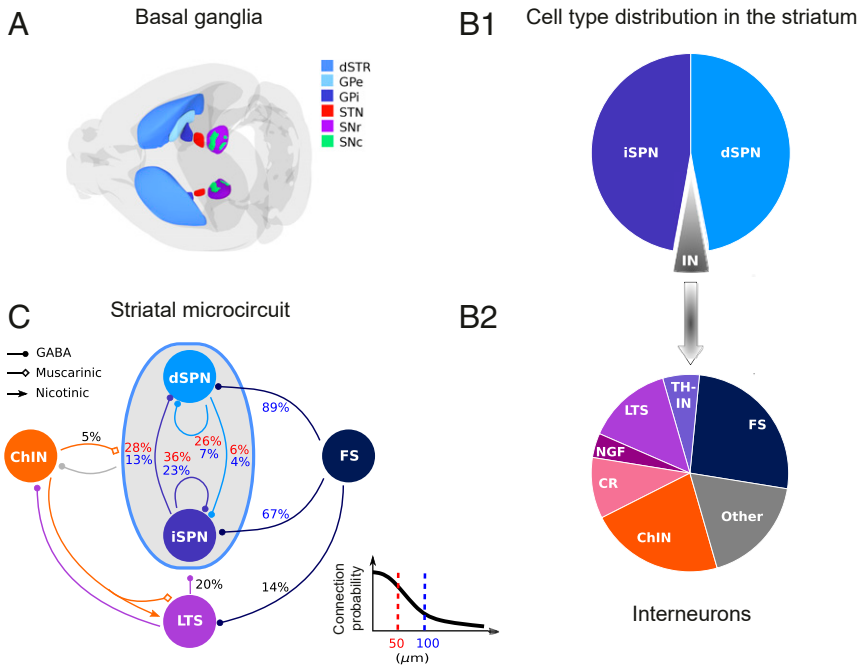

Fig. 1. Organization of the striatal microcircuit and the neuronal subtypes. (*A*) Dorsal view of the mouse brain showing the basal ganglia subnuclei. The dorsal striatum (dSTR), globus pallidus external and internal segment (GPe and GPi, respectively), subthalamic nucleus (STN), substantia nigra pars reticulata and pars compacta (SNr and SNc, respectively) are shown in relative sizes. The color coding is as indicated. (*B1*) The principal cells of the striatum are the striatal projection neurons (SPNs). They account for about 95% of all striatal neurons and form two approximately equal pools of cells that differ by their projection targets and belong to the direct and indirect pathways, dSPN and iSPN, respectively. (*B2*) The interneurons include cholinergic and GABAergic interneurons (INs) (6). By unbiased counts available for the mouse of the total number of neostriatal neurons, the parvalbumin-expressing fast-spiking (FS) cells make up 1.3%, NPY/SOM$^+$ low-threshold spiking (LTS) interneurons 0.8%, calretinin-positive cells (CR) around 0.5% in rodents, tyrosine hydroxylase-positive interneurons (THINs) 0.3%, NPY/SOM$^-$ neurogliaform (NGF) cells 0.2% and cholinergic interneurons (ChINs) 1.1%. (*C*) Schematic connectivity within dSTR involving dSPN, iSPN, FS, LTS, and ChIN. Connection probabilities within and between neuronal subtypes are shown by respective arrows; numbers in red correspond to connection probabilities for a somatic pair at a distance of 50 μm, while numbers in blue correspond to 100 μm.

other half expresses D2R, targets the GPe, and represents the indirect pathway. Neurons of this subpopulation are referred to as iSPNs. Their net effect is to further enhance the tonic inhibitory activity of the basal ganglia output nuclei.

Less than 5% of the neurons in the mouse striatum are interneurons and they can be subdivided into a number of subpopulations (pie chart in Fig. 1*B2*; ref. 6). We focus here on three important subtypes, the cholinergic (ChIN), the fast-spiking (FS), and low threshold spiking (LTS) for which the connectivity within striatum is available (Fig. 1*C*), as well as membrane properties and detailed morphology (7, 8). This means that over 98% of all striatal neurons are represented in the model.

The striatum has been studied extensively through experiments (2, 3, 7, 9). It has been characterized from the subcellular, cellular, and synaptic levels to its involvement in behavior and also through its dysfunction that occurs in a number of neurological and psychiatric diseases. To uncover the intrinsic function of striatum, simulation is indispensable, combined with detailed experimentation. Simulations spanning the subcellular—microcircuit—systems level are necessary, in order to integrate data from these different biological levels and conditions in a manner that will further enhance our understanding of function, as well as allow the formation of testable hypotheses/predictions.

Computational models addressing different aspects of the basal ganglia have been formulated on several abstraction levels, from systems level models investigating hypothesized basal ganglia "functions" or network dynamics in health and disease, using spiking networks typically simulated using ensembles of point neurons or using rate-based descriptions (e.g., refs. 10–14). These have also been validated with embodied models addressing the behavioral context (15). Approaches have also used cellular level electrophysiological and morphological data to more directly constrain detailed single neuron multicompartmental Hodgkin–Huxley models of, for example, SPNs and striatal FS interneurons (e.g., refs. 16–24). Also detailed single-neuron models exist for neurons in other basal ganglia nuclei (e.g., ref. 25). Finally, we also have models of intracellular signaling pathways activated by, for instance, dopamine or adenosine receptors (26–29).

While these models have independently investigated basal ganglia function in different anatomical contexts, a pressing need is to have a detailed common simulation platform, which allows us to integrate data from different levels of biological detail. Here, we focus on simulation at the striatal microcircuit level, in which the molecular/subcellular and systems levels meet. We present a nearly full-scale microcircuit of the mouse striatum using connectivity data, together with detailed reconstructed neuronal morphologies to create a microcircuitry mimicking the real network (see refs. 30 and 31). We populate the striatum with reconstructed neurons, with a density of 80,500 neurons/mm^3 as found in the mouse striatum and connect them together based on appositions between neurites as putative synapses, which are then further pruned to reflect available connectivity data.

The striatum has two main compartments, the striosomes and the matrix. The striosomal part (around 15% in mice) contains the same type of neurons as the matrix, but the efferent connectivity relates instead to the control of dopamine neurons, and it has different afferent input, mostly from the limbic system (32–36). The description of our simulation platform represents

the matrix compartment, the largest part of the striatum, which is concerned with the control of movements.

Results

Based on detailed experimental data, we have simulated several instances of the two subtypes of SPNs, and the ChIN, FS, and LTS interneuron types, which we report below. This has included representing the somatodendritic and axonal morphology of each subtype combined with information about membrane properties, ion channel subtypes, and so forth (*Materials and Methods* and *SI Appendix*). These data have been complemented with RNA-sequencing (RNA-seq) information (*SI Appendix*, Fig. S1 and *Materials and Methods*) regarding which subtypes of ion channels are expressed in the different cell types to obtain as precise a simulation of each cell type as possible. The single-cell models are optimized using the Blue Brain Python Optimization Library (BluePyOpt, https://github.com/BlueBrain/BluePyOpt), an extensible framework for data-driven model parameter optimization. Each model is fitted to the voltage traces recorded from the soma of a single cell. Critical features, like baseline voltage, action potential width and height, mean firing rate, etc., needed for optimization and validation of the models, are measured using the Electrophys Feature Extraction Library (eFEL, https://github.com/BlueBrain/eFEL). Models optimized for a subset of features and somatic current injections are further validated against an extended set of features and experimental protocols for subthreshold and suprathreshold current injections as discussed below (see also *SI Appendix*, *Supplementary Methods*). In the next steps, to build the microcircuit we predict the neuronal connectivity using knowledge about cell densities and dendritic and axonal morphology, and furthermore model the intrastriatal synaptic properties, and also include extrinsic inputs from cortex, thalamus, and the dopamine system. Finally, we simulate a subpart of the detailed striatal network in action, when driven from cortex, thalamus, and the dopamine system.

Simulations of Striatal Projection Neurons of the Direct and Indirect Subtype. SPNs of the direct and indirect subtypes are very similar but not identical with regard to their morphology and membrane properties (37). The iSPNs have an overall dendritic arbor that is noticeably smaller with fewer first order dendrites (38, 39) and have a somewhat higher excitability than the dSPNs. Moreover, the dSPNs express D1R and substance P, while iSPNs express D2R and enkephalin.

In Fig. 2*A* we show a dSPN reconstructed from experiments with the dendritic arbor in blue and axonal ramifications in gray. The dendrites are spiny, starting at 15 to 30 μm from the soma, reaching steady density at 50 μm, and farther out to the distal dendrites (40). The terminal branches of the dendrites represent 80% of the dendritic length (*SI Appendix*, Fig. S2). The response of the cell (red), and its simulated counterpart (black), is shown to a 1-s suprathreshold current pulse (Fig. 2*B*), and the similarity between the spike patterns of the two is clear. In Fig. 2*C*, the response to current steps is shown for several pairs of experimental and simulated cells. The control and the simulated traces establish, in each case, the close similarity in the membrane responses over the physiological range. In Fig. 2*D*, a dendritic plateau potential is produced by clustered synaptic inputs to the distal dendrites (90- to 120-μm somatic distance) leading to an activation of the voltage-dependent NMDA receptors that provide the long-lasting response in model neurons as in experiments (18). The plateau response represents a fundamental property of SPNs and most likely also contributes to plasticity. The Ca^{2+} entry due to a backpropagating action potential (Fig. 2 *E*, *Left*) in the dendritic tree has been estimated by Day et al. (41) (Fig. 2 *E*, *Right*), and it falls off within ∼100 μm from the soma in both the experimental and the simulated cell. In conclusion, the simulated dSPNs correspond closely to their natural counterparts.

The iSPNs in *SI Appendix*, Fig. S3 are presented in a similar way to that of the dSPN in Fig. 2. Individual iSPNs are very similar to dSPNs in terms of their firing properties, although there are differences in the dendritic arbor and inherent excitability as described earlier (see *SI Appendix*, Fig. S3*A* in comparison with Fig. 2*A*). They show on average higher excitability (42), as is evident from the lower rheobase in *SI Appendix*, Fig. S3*C* (compare with Fig. 2*C*). Backpropagating action potentials elicit a transient influx of calcium which decays noticeably more slowly with distance from the soma in the dendrites of the iSPNs than in dSPNs (compare *SI Appendix*, Fig. S3*E* and Fig. 2*E*). The ability to generate plateau potentials in response to clustered glutamatergic synaptic input is, however, shared between dSPNs and iSPNs (*SI Appendix*, Fig. S3*D*).

Simulation of FS Interneurons. FS interneurons represent around one-fourth of the striatal interneuronal population and express parvalbumin and have no spines. They have short-lasting action potentials and show little spike frequency adaptation. They inhibit SPNs of both types in the nearest few hundred micrometers from the soma (43) and to a lesser degree also LTS interneurons (44). The reconstruction of one FS in Fig. 3*A* shows the wide dendritic arbor (blue) and the axonal ramifications (gray) (*SI Appendix*, Table S4). FS interneurons are also connected with each other through gap junctions, as well as GABAergic synapses (21, 45, 46).

The simulated FS cell has the corresponding characteristics, and its electric response is shown in Fig. 3*B*, in which the response of the model and its biological counterpart to both depolarizing and hyperpolarizing current steps are shown separately. Fig. 3 *C*, *Left* shows the subthreshold current–voltage response for four experimental neurons (red traces) and the corresponding data for the model neurons, which are very close to each other. Similarly, the frequency–current responses overlap with the experimental data for the four model neurons as illustrated.

Simulations of LTS Interneurons. The LTS interneurons are spontaneously active GABAergic interneurons, representing around 20% of all striatal interneurons. The LTS population can be further subdivided based on expression of somatostatin (SOM), nitric oxide synthase (NOS), and neuropeptide Y (NPY). Whether all these subpopulations express the same "classical" electrophysiological phenotype of LTS interneurons is unknown at present (8, 47).

LTS interneurons (Fig. 4*A*) have a medium-sized soma (9 to 25 μm), sparse dendritic arborization with three to five primary dendrites, and the least dense but largest axonal arborization of all striatal neurons which can extend in straight lines for up to 1 mm (8).

Fig. 4*A* shows the reconstructed morphology of an LTS neuron with dendritic arborizations (in blue) and a reconstructed axon (in red). It is similar to previously described LTS cells (*SI Appendix*, Table S5). A characteristic electrophysiological feature of the LTS cells is their high input resistance and large membrane time constant (Fig. 4*B*), with high variability in subthreshold voltage–current relation (Fig. 4*C*). The multicompartmental model of the LTS was constrained using responses to somatic square-pulse current injection data. The model and the data show similar membrane responses during both subthreshold (Fig. 4*B*) and suprathreshold (Fig. 4*D*) activation.

Simulation of ChINs. The cholinergic population represents roughly one-fourth of the striatal interneuron population. ChINs lack spines and were referred to as large aspiny interneurons in

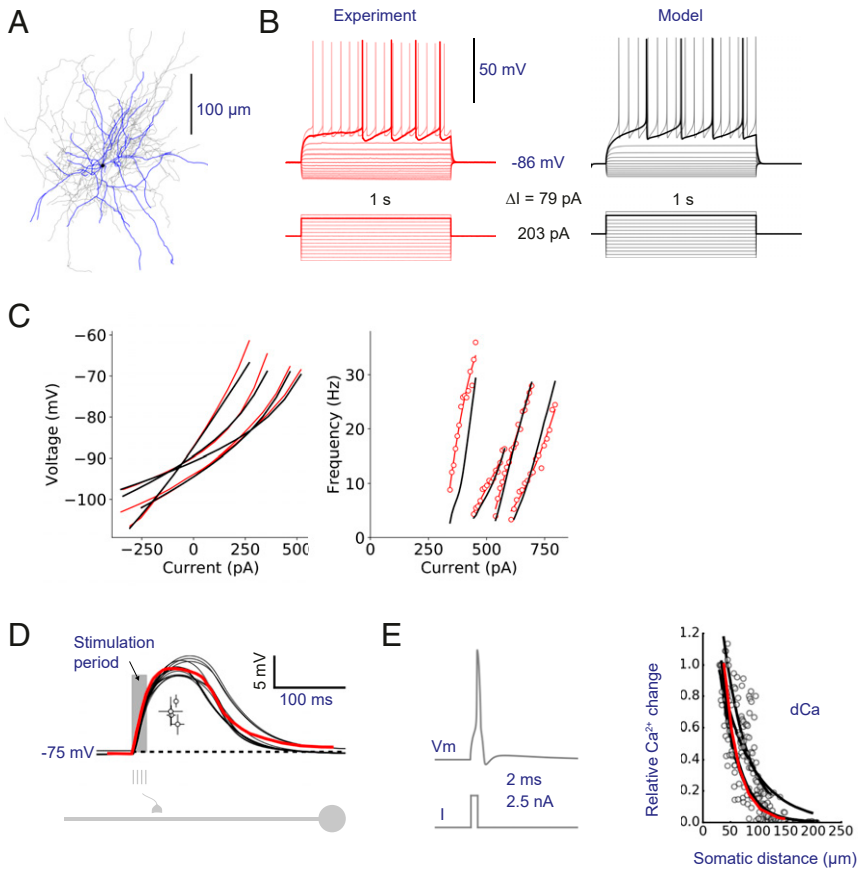

Fig. 2. The direct pathway striatal projection neuron (dSPN) expressing dopamine D1 receptors. (*A*) Neurolucida reconstruction of a single dSPN with dendrites (blue) and axon collaterals (gray). Black dot marks the soma. (*B*) Sub- and suprathreshold responses to current injections for a model neuron (black) and the corresponding experimental data (red). An example model fit to experimental data, with the current protocol used; holding current 203 pA to keep the baseline membrane potential around −86 mV. (*C*) Population behavior for models and experiment: voltage–current and frequency–current relations shown for four dSPNs optimized to corresponding data. (*D*) Somatic potential response to spatiotemporal clustered synaptic input, demonstrating the model's ability to trigger NMDA-dependent plateau potentials. The dots in the middle give the mean midpoint (half duration, half amplitude) of the plateaus triggered at a somatic distance of 90 to 120 µm. Experimental data (red) digitized from ref. 18. (*E*) Normalized change in calcium concentration in response to a backpropagating action potential (triggered with a short duration 2-ms high amplitude 2.5-nA current injection). Experimental data are extracted from ref. 41. Model data are in black, experimental data in red.

earlier studies (48). They act via both nicotinic and muscarinic receptors and target both types of SPNs, LTS, FS, and also the presynaptic axon terminals of dopaminergic neurons from SNc (49). The ChINs are spontaneously active as has been shown in both in vitro and in vivo recordings in rodents (3 to 10 Hz in vivo) (50–52) and also identified as the tonically active neurons (TANs) in primates (53–55). They are known to pause during dopamine bursts, as well as during behaviorally salient stimuli and receive input from dopamine neurons and thalamic afferents (55–58).

The multicompartmental model of the ChIN was constructed using detailed morphology (Fig. 5*A*) along with ion channel models (*SI Appendix*, Fig. S1). ChINs have a dendritic arbor extending over ∼200 µm and the dendrites have fewer bifurcations as compared to SPNs and FS neurons with around four primary dendrites (based on 10 detailed reconstructions). The same neuron as in Fig. 5*A* was stimulated with different experimental protocols to capture both subthreshold and suprathreshold responses (*Materials and Methods*). These protocols were used to optimize the conductances of the multicompartmental model with that of the biological counterpart. The optimized model is shown in Fig. 5*B* together with examples of the subthreshold responses to current step injections, which largely reproduces the biological counterpart (red trace) with a prominent I_h current characteristic of ChINs (59, 60). The spiking responses produced by suprathreshold current steps in both the experimental and the simulated cells are similar (Fig. 5*D*). Additionally, the model also reproduces other behaviors like postinhibitory rebound spiking, illustrated in the simulated cell in Fig. 5*C*, as well as the pause response (Fig. 5*E*) reported in several experiments as noted above.

Dopaminergic Modulation of SPNs, FSs, LTSs, and ChINs. An important aspect of striatal connectivity and function is the dopamine innervation. The simulated dSPNs, FSs, and LTSs are equipped (see *Materials and Methods*) with depolarizing dopamine receptors of the D1 type (D1R), whereas iSPNs and ChINs instead have inhibitory D2Rs as their biological counterparts. Fig. 6*A* shows the increased activity of dSPNs and FSs when dopamine is applied (gray trace) and the opposite effect with decreased activity for iSPNs and ChINs. Fig. 6*B* compares the response of different subtypes of experimental and model neurons to dopamine application and affirms the similarity between the response of model neurons with that of their experimental counterparts. These neuromodulated model neurons are incorporated into the striatal microcircuit simulations below.

Distributing Cells and Predicting Intrastriatal Synapse Statistics. The dorsal striatum has a comparatively homogeneous cellular

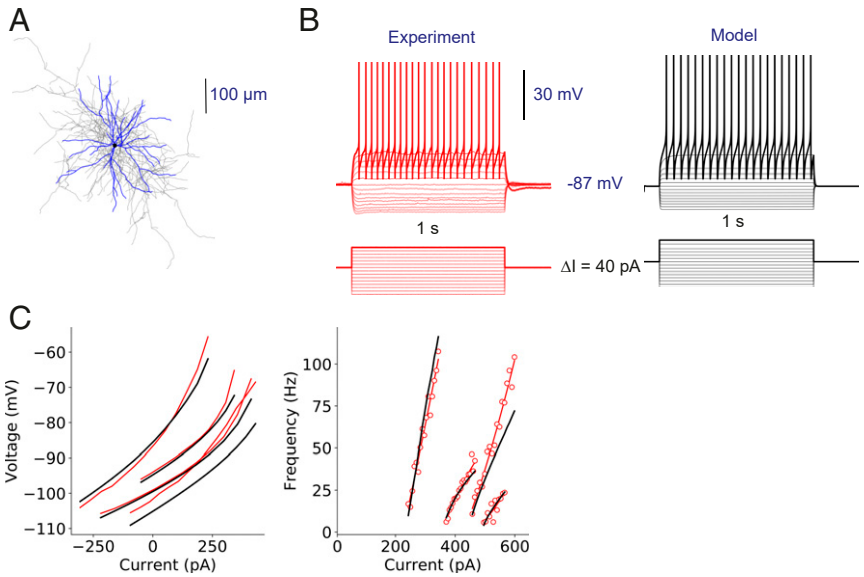

Fig. 3. Model of fast-spiking (FS) interneuron fitted to the recordings from the dorsolateral striatum. (*A*) Neurolucida reconstruction of a single FS (number of reconstructions, $n = 4$) with dendrites (blue) and axon collaterals (gray). Black dot marks the soma. (*B*) Somatic response to square-pulse current injections for the duration of 1 s with increment of 40 pA in a recorded cell (red) and corresponding model (black). Holding current of 229 pA provides the baseline voltage around −87 mV. (*C*) Fit of the models to the recorded parvalbumin-positive cells ($n = 4$), subthreshold voltage–current relation (*Left*), and suprathreshold frequency–current response (*Right*). Model data are in black, experimental data in red.

composition, with cell density following continuous spatial gradients specific for each cell type (61–65). No clear anatomical distinction has been made between the functionally specialized areas of the striatum selective for different cortical and thalamic afferents (66–69). Despite the growing evidence of multifaceted compartmentalization of the dorsal striatum (70–73) its functional structure remains largely unmapped. The striatum has a well-established subdivision of the matrix and striosome (patch) compartments with over 60 known molecular markers (32). Our cell placement algorithm supports multiple volumes, and the

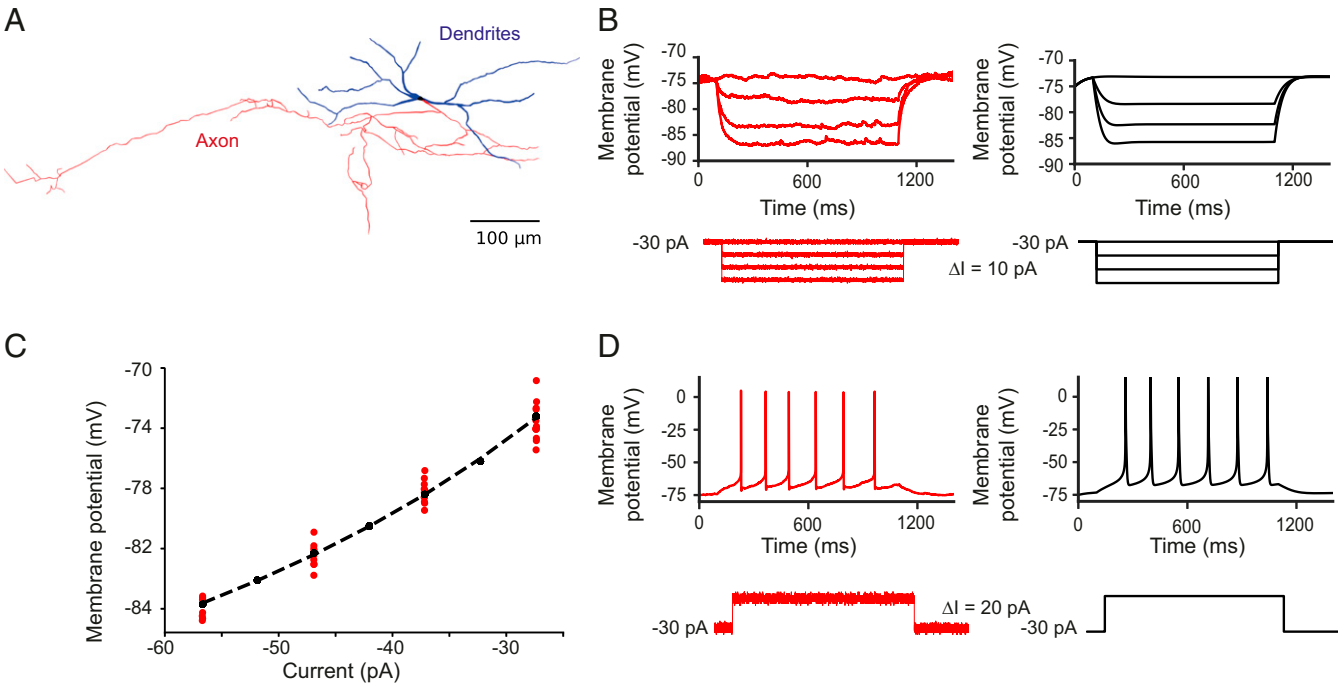

Fig. 4. Low-threshold spiking (LTS) interneuron. (*A*) Neurolucida reconstruction of a single LTS with dendrites (blue), axon collaterals (red) and soma (black). (Scale bar, 100 µm.) (*B* and *D*) Response to somatic hyperpolarizing and depolarizing current injections in a recorded cell (red) and corresponding model neuron (black). (*C*) Set of nine experiments performed on the same cell (red dots) emphasize the high membrane potential variability in response to similar current amplitude (the difference in the current injection is in the order of a few hundredths of picoampères). Model data are in black, experimental data in red.

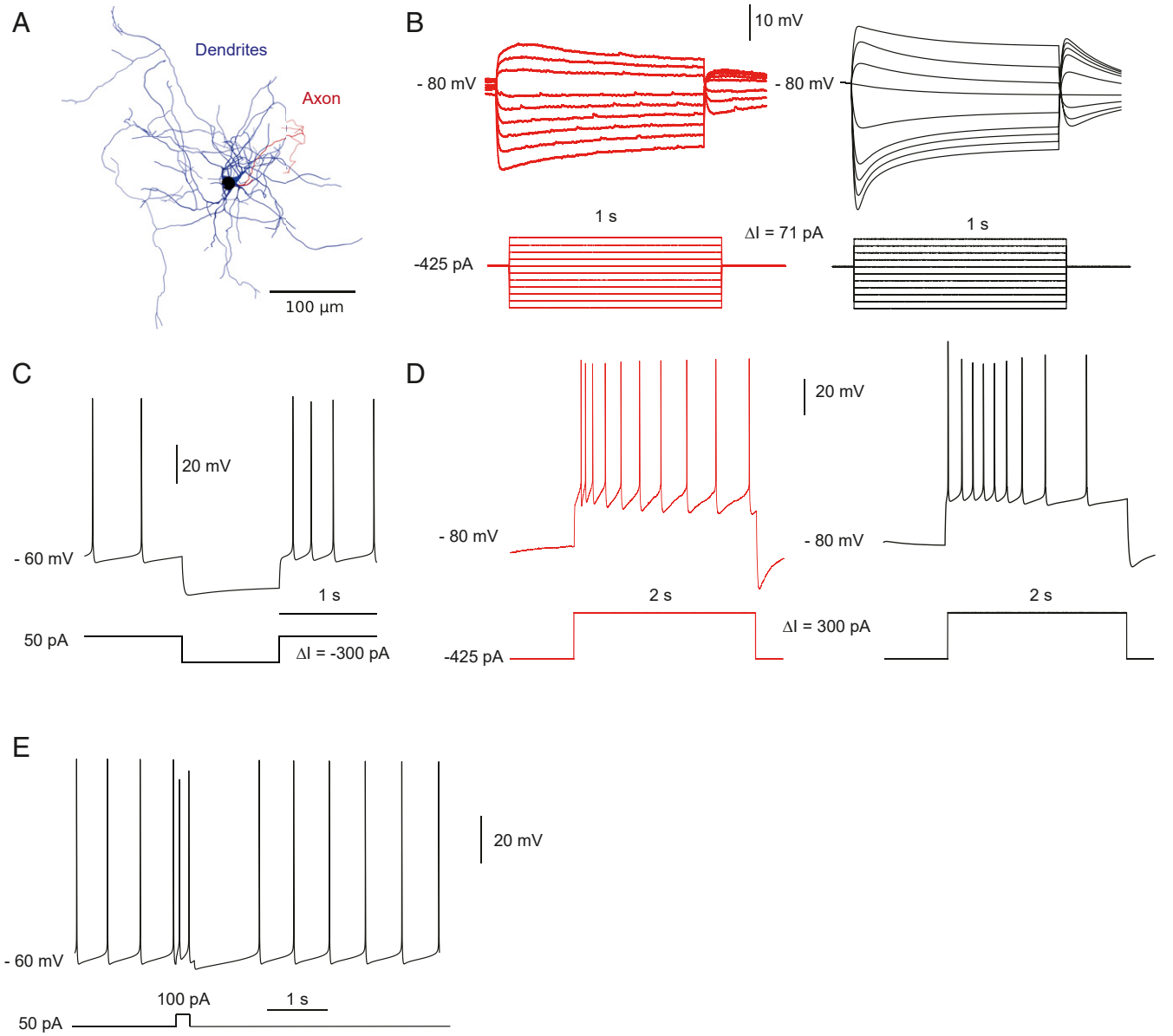

Fig. 5. Cholinergic interneuron (ChIN) model. (*A*) Neurolucida reconstruction of a cholinergic interneuron with dendrites (blue), axon collaterals (red), and soma (black). (Scale bar, 100 µm.) (*B*) Intravenous protocol in experiment (red) and model (black). (*C*) Hyperpolarizing current injection to illustrate the rebound behavior in the model. (*D*) Responses to suprathreshold current injection in the model (black) and the experiment (red). (*E*) Injected depolarizing current of 100 pA for 300 ms during activity, to illustrate the pause response in the ChIN model.

striosome/matrix division can be included in the future versions of the simulation platform based on high-resolution volume definitions of the two striatal compartments (71, 72, 74).

The neurons are placed with appropriate cell density randomly within the simulated volume of the striatal tissue (Fig. 7 *A*–*C*), with a small exclusion zone, to avoid overlap of the somas. The mouse striatum is around 21.5 mm^3 (Allen Mouse Brain Atlas; mesh data from C57BL/6J mouse, shown in Fig. 7*A*) with a total of 1.72 million neurons (75), which corresponds to a density of 80,500 neurons/mm^3. The cell populations (Fig. 1*B*) were subdivided assuming 47.5% dSPNs, 47.5% iSPNs (6, 76, 77), 1.3% FS, 1.1% ChINs (78), and 0.8% LTS (79). Thus, over 98.2% of the striatal neurons were represented in the simulation.

The striatal circuitry shown in Fig. 1*C* is generic for the entire structure with connection probabilities representing average values established in multiple experiments (43, 44, 47, 80, 81).

The GABAergic connections between the SPNs make up the majority of the intrastriatal circuit connectivity, although with relatively high failure rate, 70% for dSPNs and 40% for iSPNs (81, 82). Generally, iSPNs demonstrate higher probability of forming synaptic connections than dSPNs (within 50-µm distance from the soma): dSPN–dSPN 26%, dSPN–iSPN 6%, iSPN–dSPN 36%, iSPN–iSPN 28% (n = 105) (81). This pattern of connectivity is preserved over a larger distance, up to 100 µm between the cell somata (n = 294): 7% dSPN–dSPN and 4.5% dSPN–iSPN pairs against 23% iSPN–iSPN and 13% iSPN–dSPN pairs (43).

FSs provide strong and very reliable inhibition (with a low failure rate <1%) of the projection neurons with connection probability biased toward dSPNs, which have a denser dendritic field, 89% FS–dSPN versus 67% FS–iSPN connected pairs within 100 µm of lateral distance (43). The FS–SPN synapses are

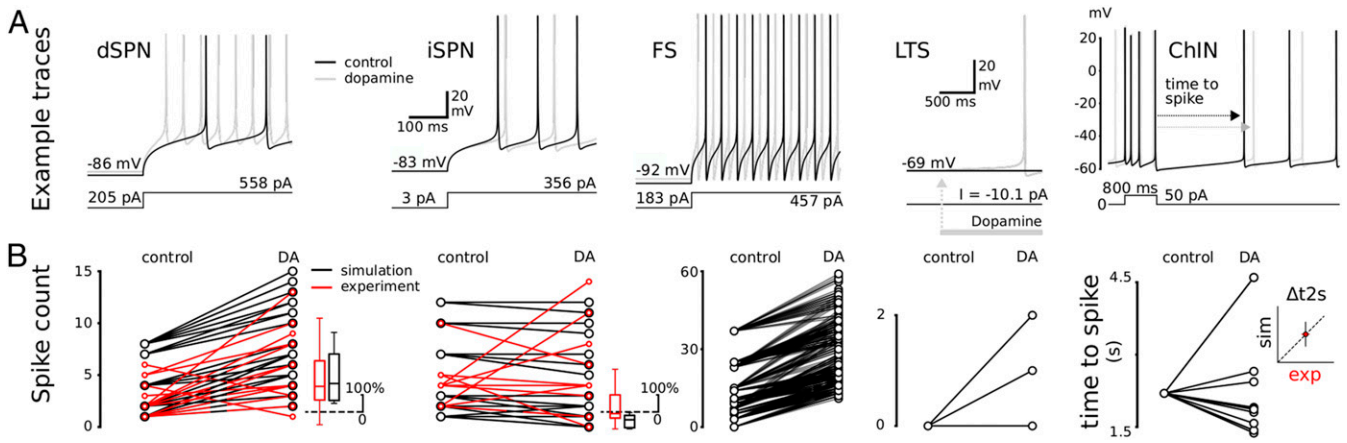

Fig. 6. Dopamine modulation of simulated striatal cells. (*A*) Representative traces of simulated cells (dSPNs, iSPNs, FS, LTS, and ChINs) are shown under control conditions (black) and during simulated bath application of dopamine (gray traces). The response to a depolarizing current pulse is shown for each cell type before and after dopamine. For ChINs, the time to spike following a burst-pause protocol is used to quantify the modulation and for LTS dopamine-induced depolarization from −60 mV is used. For the other cell types, spike counts following a step depolarizing current is used (four protocols per model and four models per cell type). For LTS, dopamine is present only during a certain time period (see bar), whereas for all other simulations, dopamine is present throughout the simulation. (*B*) Population data for each type of neuron shown together with comparisons against experimental data for control conditions and with dopamine (42, 110). *Insets* show relative activity.

predominantly located proximally, where they have a strong influence on the activity of the SPNs (77, 83–85).

LTS interneurons receive synaptic contacts on their proximal dendrites from both FSs and ChINs. The connection probability between FSs and LTSs is around 14% (44). The major efferent target of LTSs is the SPNs. Axon terminals form symmetric synapses on 20% of the SPNs (8, 47), mostly on the distal region of the dendrites and on spines, largely avoiding the soma (85–89). Optogenetic experiments have shown that LTSs form GABAergic synapses onto distant ChINs inhibiting them through $GABA_A$ receptors (90). In addition, there is evidence suggesting that LTSs can induce slow depolarizations in cholinergic interneurons mediated by nitric oxide (91). LTSs also receive monosynaptic excitatory input from cortex, but not from thalamus (parafascicular nucleus [PFN]) that instead inhibits LTSs, most likely mediated via the GABAergic THINs (7) and ChINs by means of M4 muscarinic acetylcholine receptors (92).

ChINs are distributed relatively uniformly, making a dense neuropil throughout the striatum (63). ChINs affect the striatal circuit via either nicotinic or muscarinic receptors. The ChIN-to-SPN connection is primarily muscarinic, where both M1 and M4 receptor subtypes are expressed, with dSPNs expressing both types while iSPNs express mainly M1 receptors (93). The ChIN-to-LTS connection contains both a nicotinic and muscarinic component with an inhibitory net effect (92) (Fig. 1*C*). The FS interneurons are excited by nicotinic receptors but muscarinic receptors on presynaptic GABAergic terminals attenuate the inhibitory input (94). The main recipients of nicotinic excitation from ChINs are the neurogliaform NPY-expressing interneurons (NGFs) (95) and subtypes of the 5HT3a-expressing interneurons (7, 47, 96, 97).

The synapse placement is divided into two steps (Fig. 7*D*). In the first step a voxel-based touch detection algorithm marks where in space the axon, dendrites, and soma are located and then it places putative synapses where two different axonal and dendritic processes or somata are in close proximity. In the second step, the sets of putative synapses are pruned to match the experimentally observed connection probabilities (*Materials and Methods*).

All these steps are probability based, and together they allow the pairwise connection probability as shown in Fig. 8*A*, number of synapses between coupled pairs (Fig. 8*B*), number of connected neighbors (Fig. 8*C*), and the synapse density along the dendrites (Fig. 8*D*). Additional figures for the connections

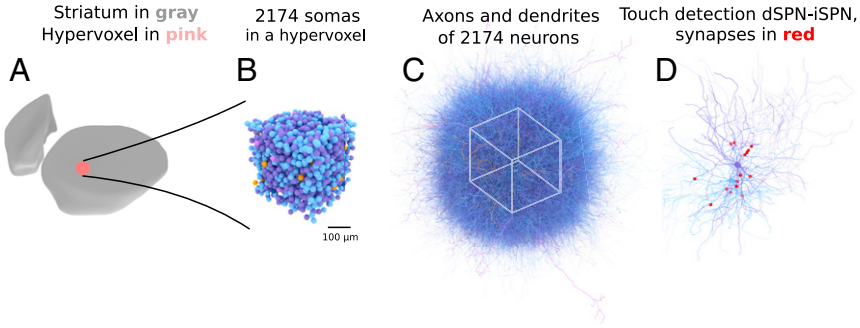

Fig. 7. Synapse placement using touch detection algorithm. (*A*) Striatal three-dimensional (3D) mesh in gray, the touch detection is parallelized, and each process handles a subset of the space, here shown as a cube (hypervoxel, see *Materials and Methods*). (*B*) The somas of all of the neurons within the hypervoxel, ~2,174 neurons. (*C*) Axonal and dendritic arborization of the 2,174 neurons. (*D*) Touch detection of two neurons using 3-µm voxel resolution. Synapses are shown in red.

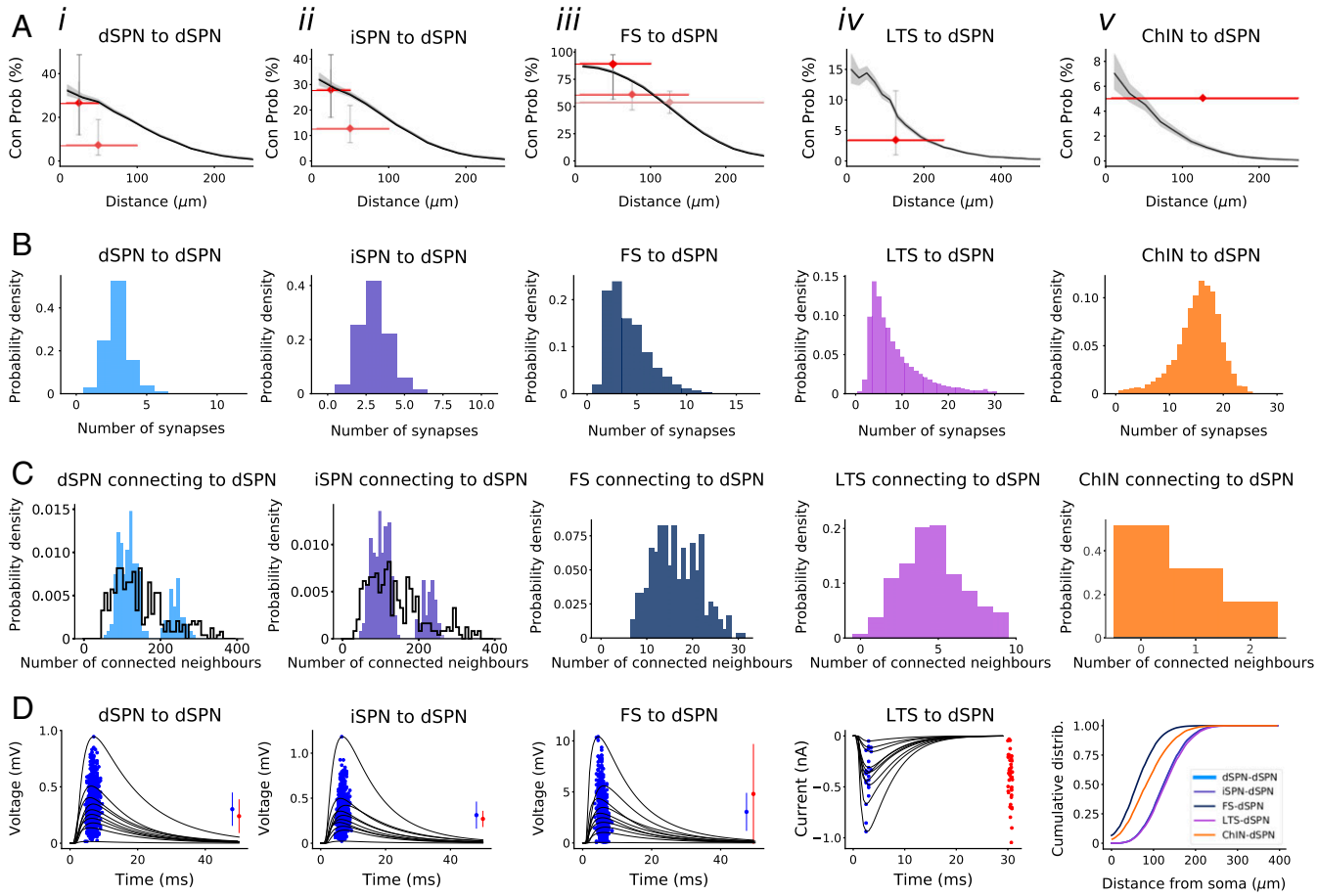

Fig. 8. Statistics of connections projecting to dSPN in the striatal microcircuitry. Connections shown for (*i*) dSPN–dSPN, (*ii*) iSPN–dSPN, (*iii*) FS–dSPN, (*iv*) LTS–dSPN, and (*v*) ChIN–dSPN. (*A*) Pairwise connection probability for the different neuron types projecting to dSPN. Black curve corresponds to the simulated network and gray region shows the Wilson score (111) for the model. Red line shows experimental data with error bars showing the Wilson score, and the line length indicates spread of lateral distance between connected neuron pairs. Experimental measurements were made for neuron pairs within 50-μm distance (*A*, *i–iii*) in ref. 81, 100-μm distance (*A*, *i–iii*) in ref. 43, 250-μm distance (*A*, *iii* and *iv*) in ref. 112, and 250-μm distance (*A*, *v*) in ref. 80. (*B*) Distribution of number of synapses between individual connected neuron pairs. The pairs are indicated above each graph in *i–v*. (*C*) Distribution of number of connected neurons for each type of presynaptic neuron. The connectivity between presynaptic to postsynaptic neuron is indicated above each graph in *i–v*. Here we show statistics for neurons in the center of the volume to avoid edge effects. Note that the bimodal distribution seen here is a consequence of only using a limited number of morphologies for dSPN and iSPN. Preliminary modeling shows that adding a larger number of reconstructions creates a unimodal distribution; however, currently we only have optimized models for the morphology of four dSPNs. Future versions will include more reconstructions. (*C*, *i* and *ii*) The black line shows the distribution obtained for a larger set of reconstructions ($n = 100{,}000$) using a jitter to promote morphological variability (see also *SI Appendix*, Fig. S4). (*D*, *i–iii*) Response in a dSPN when a presynaptic (*i*) dSPN, (*ii*) iSPN, and (*iii*) FS is activated. Blue dots mark peaks of postsynaptic potentials. (*Insets*) Mean and SD for model peaks (blue) and experimental data (red) from Planert et al. (43). (*i* and *ii*) With a chloride reversal potential of −40 mV and (*iii*) from Straub et al. (90) with a chloride reversal of 0 mV. (*iv*) Response in dSPN when LTS neurons are activated. Model peaks are marked with a blue dot, experimental peaks (90) marked with red dots (*Inset*). (*v*) Cumulative distribution of synapses on the dendrites as a function of the distance from the soma. Connection statistics for other neuron pairs are shown in *SI Appendix*.

between the other striatal neuron pairs are available in *SI Appendix*. This pruning scheme is similar to that of Markram et al. (31). Gap junctions are handled in a similar way.

One strength of a microcircuit model is that it allows us to check the consistency of cellular and network level data. For example, to match experimentally observed voltage deflections for pairwise connection strength between SPNs (Fig. 8 *A*, *i* and *ii*) (43) while maintaining the experimentally observed connection probabilities (Fig. 8 *A*, *i* and *ii*) (43, 81), synapse strength, and failure rates (81), we had to reduce the fraction of proximal synapses. And indeed, having the inhibitory SPN–SPN synapses located more distally appears to have support in the literature (98). In the case of LTS to dSPN, there were no data available for the number of synapses between pairs, but data existed for the response in dSPN to optogenetic activation of neighboring LTS (90, 99). To match this data, we had to increase the connection probability and the number of synapses (Fig. 8 *A*, *iv*). The corresponding information to that shown in Fig. 8 is shown for inputs to iSPNS, FS, LTS, and ChINs in *SI Appendix*, Figs. S4–S7.

Properties of the Dynamic Models of Intra- and Extrastriatal Synapses. Repetitive activation of synapses can lead to either facilitation or depression of the response over short time scales. To characterize the dynamics of intrastriatal synapses (43), as well as corticostriatal and thalamostriatal synapses (100), a protocol with eight pulses at 20 Hz followed by a recovery pulse, after a delay, was used. The short-term plasticity of cortico- and thalamostriatal inputs was extracted during bath application of gabazine to avoid the recruitment of local inhibitory pathways. We then fit the parameters of a Tsodyks–Markram model to the

dynamics, to match the facilitation and depression observed experimentally. See *Materials and Methods* for details.

Fig. 9 *A*, *i–iv* show the synaptic input to dSPNs from the motor area (M1) on both sides, the ipsilateral somatosensory area (S1), and from thalamus, and in Fig. 9*B* the input from dSPNs, iSPNs, and FS to dSPNs are shown. The experimental data are shown in red and matching simulation data in black. Whereas the afferent input to dSPNs from several sources are depressing, including the contralateral M1, they are facilitating from thalamus and other dSPNs. Examples of the corresponding data for synaptic input to iSPNs, FSs, LTSs, and ChINs are shown in *SI Appendix*, Figs. S8 and S9. In conclusion, we have for each of the many types of synapses adapted the dynamic properties to make the model synapse match its biological counterpart for each of the many input synapses.

Simulation of the Striatal Microcircuit with Cortical, Thalamic, and Dopaminergic Input. In Fig. 10, we have integrated the previous simulations of the cellular and synaptic properties to form a striatal microcircuit simulated as a large-scale network with altogether 10,000 neurons, representing dSPNs, iSPNs, FSs, LTSs, and ChINs in proportion, as described in detail above (Figs. 1–9 and *SI Appendix*, Figs. S1–S8). They were distributed with appropriate cell density, dendritic and axonal ramifications, and synaptic properties (after pruning 6.46 million synapses). The network was driven by cortical and thalamic glutamatergic input with dynamics matching experiments (Fig. 9 and *SI Appendix*, Figs. S8 and S9). Fig. 10 *A* and *B* shows a simulation, in which there is a thalamic and cortical low level input throughout the simulation. In addition, there is a high level cortical input, which activates both dSPNs, iSPNs, FSs, and LTSs, but not ChINs (Fig. 10 *A* and *B*; cortex command [crtx cmd]). A modulatory signal was also added in the form of a short period of dopaminergic activation (DA). During this signal, the dSPN and FS populations expressing D1R were further activated, while iSPNs and ChINs that express D2Rs were inhibited, as were LTSs. ChINs marked the end of the dopaminergic signal with increased activity (postinhibitory rebound).

Discussion

This study provides a microcircuit model of striatum with greater granularity than has ever been presented earlier. We have represented over 98% of the striatal neurons with appropriate cell density, representative somatodendritic and axonal morphology, membrane properties, synaptic connectivity, and short-term dynamics. We have thus modeled the two types of SPNs, ChINs, FSs, and LTSs, each with their own particular membrane properties. Moreover, we include cortical, thalamic, and dopaminergic input that can target specific modules within striatum. Although not implemented at present, the selective glutamatergic input from the PPN to the interneurons can easily be achieved, as well as the inhibitory inputs from the GPe and midbrain to striatal neurons. A further strength is that SPNs can respond with long-lasting dendritic plateau potentials, dependent on NMDAR activation from, e.g., corticostriatal input as an important factor for inducing synaptic plasticity (18, 101).

We thus have developed a first draft in silico model of striatum with most types of neurons modeled with their cellular interaction under resting conditions, and with the possibility to provide input to the entire striatum or part thereof from cortex, thalamus, and the dopamine system. The readout can be the dSPNs promoting action, and the iSPNs having an inhibitory effect, although they are often activated together, but not with identical patterns (3, 102, 103). The intention with the model is to be able to test different combinations of input to different classes of interneurons during concurrent activation from other inputs. For instance, the ChINs receive input from thalamus, only weak input from the cortex (100), and they are important players for striatal function. Similarly, the LTSs are disynaptically inhibited from thalamus (7, 47) but receive strong input from the motor cortex (61, 100). The glutamatergic neurons of PPN activate all interneurons but not SPNs (104), and the list can be made very long. We have in *SI Appendix* information links to all of the neuronal and synaptic data used, and also the model building process is outlined in detail. Thus, when new data accumulate, the model can be further improved and validated such as the additional interneuron subtypes where current quantitative data are still insufficient. For example, data for additional

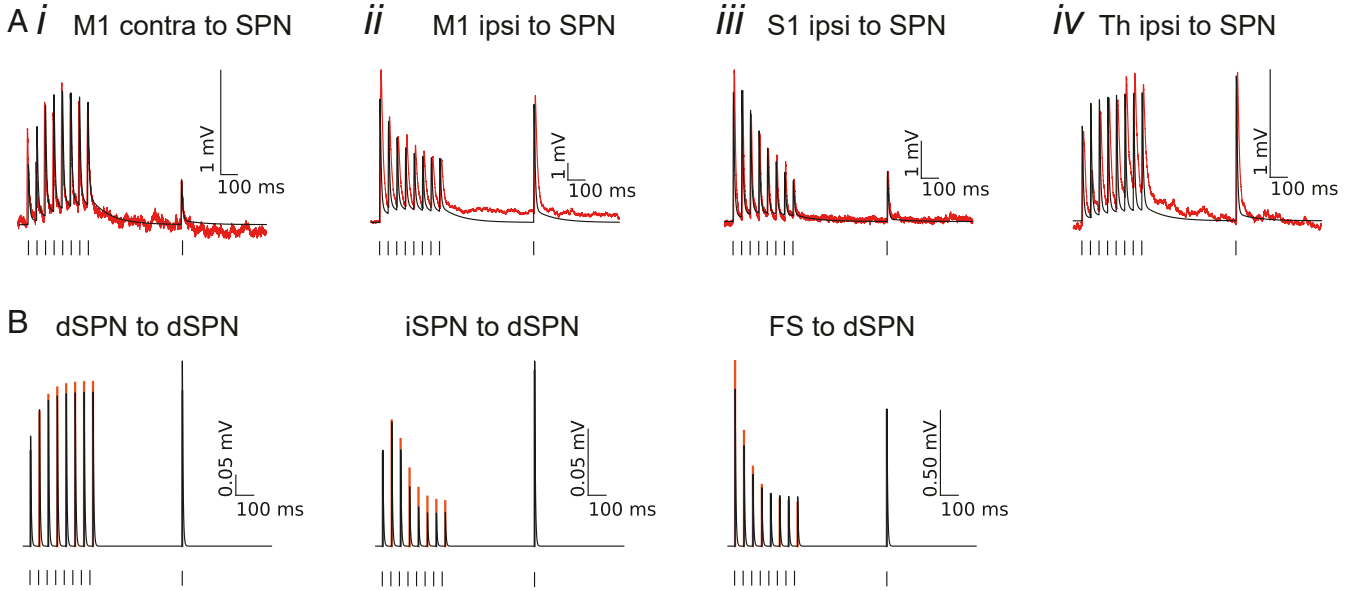

Fig. 9. Fitting SPN synaptic dynamics. The Tsodyks–Markram model was fitted using a single compartment. (*A*) Example response traces of optogenetic activation of cortical and thalamic input (100). Black trace is model; red trace is experimental data. Protocol includes eight pulses at 20 Hz followed by a recovery pulse. (Scale bars, 1 mV and 100 ms.) (*B*) Synaptic connections between dSPN and dSPN, iSPN and FS. Black line is model; orange line is surrogate data (*Materials and Methods*). See *SI Appendix*, Figs. S8 and S9 for additional examples on intrastriatal and extrastriatal synaptic inputs.

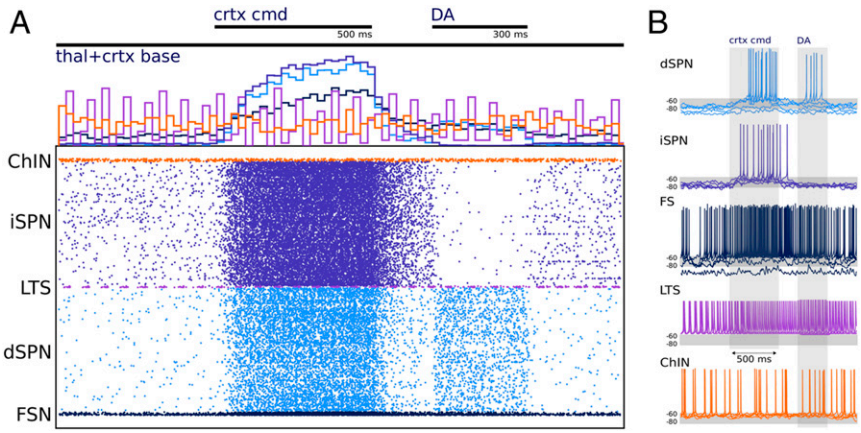

Fig. 10. Network simulation of 10,000 neurons. (*A*) The activity of the network is shown in the form of a raster plot (*Bottom*) and spike histogram (*Top*). (*B*) Example traces of each cell type in the network are shown. The network is driven with cortical and thalamic input and modulated by dopamine, as indicated at the *Top* of the figure and the shaded areas (in *A* and *B*, respectively). The three inputs represent 1) baseline activation of cortical and thalamic input (thal+crtx baseline), 2) a cortical command signal (crtx cmd), during which the cortical activation is increased (given to all cells except the ChINs), and 3) a dopaminergic modulation signal that acts on conductances in accordance with Fig. 6, *SI Appendix*, Tables S7–S10, and Lindroos et al. (106).

quantitative validation of the effective interactions at the network level of the different types of synaptic projections, from the pool of different interneuronal subpopulations to postsynaptic dSPNs and iSPNs, would be very valuable.

What are the limitations of the current platform? As mentioned above, certain subtypes of striatal interneurons with less detailed information such as the THINs, NGF, and 5HT3a interneurons (47, 96) have not yet been incorporated into our simulation. Additional classes of interneurons can and will be added according to data availability from experimental groups. Disynaptic inhibition between ChINs (105) is also not yet implemented, as well as the slower metabotropic synaptic connections such as responses to cholinergic inputs via muscarinic receptors (99). The striosome/matrix division is not represented here but can be included in the future versions of the simulation platform. Synaptic plasticity is not yet implemented, and this is obviously a critical element when considering reward and reinforcement learning. An example of how to integrate a receptor-induced cascade affecting membrane or receptor properties is already explored in Lindroos et al. (106) and in future work can be introduced also into the microcircuit platform. A further limitation of these models is that we have not implemented dendritic spines, which represent one major structure for synaptic plasticity (long-term potentiation [LTP]), and neither have we modeled presynaptic long-term depression (LTD). This would, however, be very demanding from a computational perspective and neither is included in contemporary data-driven simulations so far of cortical, including visual cortex, cerebellar, or hippocampal microcircuits (see, e.g., refs. 30, 31, 107, and 108).

With regard to the input from cortex we know that different areas of cortex project to different parts of striatum, and that the input is shared between the collaterals of midbrain and brainstem projecting pyramidal tract neurons (PT) and that of neurons with an intratelencephalic projection (IT). The latter can carry information from the contra- or ipsilateral hemisphere both within cortex and to striatum but not further caudal, to the brainstem. We also know that cortex can provide strong input from selected areas in the context of the generation of behavior, but our knowledge of the relative contribution of IT and PT neurons and possibly selective inputs to different cell types remains less clear from a behavioral perspective, but the striatal platform will allow us to experiment with different combinations of inputs.

Concluding Remarks. We will facilitate the active usage of the current striatal platform by exporting the model into SONATA (109), which also makes the model runnable on the EBRAINS brain simulation infrastructure (https://ebrains.eu). In summary, well-constrained microcircuit models, as the one presented here, will be valuable as platforms for simulating phenomena at both a lower and higher resolution. For example, activity-dependent synaptic plasticity may be simulated by integrating subcellular level models of receptor-induced signaling predictive of plasticity into dendritic compartments of relevant neuron types, and the effect on the network activity can be explored. In silico experimentation with this detailed platform will be reported in a forthcoming study regarding mechanisms of action—selection and the contribution of each of the different neuronal populations (deletions, amplification), synaptic properties, and plasticity. Also, local field potentials (LFPs) and other measurables resulting in dynamic phenomena can be synthesized from the model. Furthermore, cellular-level changes as seen in disease (e.g., Parkinson's disease, ref. 81) can be implemented and the consequences investigated to both better understand symptoms causing mechanisms, as well as predict compensatory factors. Hypotheses regarding how striatum can perform its functions can be explored with the model, and cellular-level mechanisms assumed to be important for supporting such processing, such as dendritic plateau potentials, can be investigated. Last but not least, the striatal modeling platform can be combined with detailed cortical models (31) and could facilitate investigations of corticostriatal interaction at an unprecedented level of biological detail in various forms of experimental paradigms.

Materials and Methods

All animal procedures were performed in accordance with the national guidelines and approved by the local ethics committee of Stockholm, Stockholm Norra djurförsöksetiska nämnd, and in accordance with the European Communities Council Directive of November 24, 1986 (86/609/EEC), under an ethical permit to G.S. (N12/15).

The modeling of the striatal microcircuitry consists of several steps: 1) experimental data acquisition, 2) morphological reconstruction and optimization of electrophysiological models for the neurons, 3) placement of the neurons and synapse prediction in silico, 4) constraining the synaptic properties and generating input for the model, and 5) simulating the microcircuitry. This striatal model is hosted in EBRAINS (https://kg.ebrains.eu/search/instances/Model/a6458de3-a176-4378-9b03-34a26f5da3bd); constraining data and code are publicly available on GitHub (https://github.com/

hjorthmedh/Snudda) and through the HBP platform (detailed information about modeling and experiments is included in *SI Appendix*).

ACKNOWLEDGMENTS. We are grateful for the invaluable comments and advice from Dr. Brita Robertson and Prof. Sten Linnarsson for sharing data prior to publication. The support of the Swedish Medical Research Council (Grants VR-M-K2013-62X-03026, VR-M-2015-02816, and VR-M-2018-02453 to S.G.; Grant VR-M-2017-02806 to J.H.K.; and Grant VR-M 2015-02403 to G.S.); European Union Seventh Framework Programme (Grant FP7/2007-2013) under grant agreement 604102 (HBP); EU/Horizon 2020 Grants 720270 (HBP SGA1) and 785907 (HBP SGA2) to S.G. and J.H.K.; National Institute on Alcohol Abuse and Alcoholism Grant 2R01AA016022 to J.H.K.; the Knut & Alice Wallenberg Foundation (Grant KAW 2014.0051) to G.S.; the European Research Council (Grant ERC 282012) to G.S.; the Swedish Brain Foundation (Hjärnfonden Grant FO2018-0107) to G.S.; the Karolinska Institutet Strategic Program for Neuroscience to G.S.; Karolinska Institutet doctoral funding for A.T.; and the Karolinska Institutet to S.G. is gratefully acknowledged. The simulations were performed on resources provided by the Swedish National Infrastructure for Computing at PDC (Center for Parallel Computing) Center for High Performance Computing.

1. A. M. Graybiel, The basal ganglia: Learning new tricks and loving it. *Curr. Opin. Neurobiol.* **15**, 638–644 (2005).
2. A. M. Graybiel, Habits, rituals, and the evaluative brain. *Annu. Rev. Neurosci.* **31**, 359–387 (2008).
3. A. Klaus, J. Alves da Silva, R. M. Costa, What, if, and when to move: Basal ganglia circuits and self-paced action initiation. *Annu. Rev. Neurosci.* **42**, 459–483 (2019).
4. S. Arber, R. M. Costa, Connecting neuronal circuits for movement. *Science* **360**, 1403–1404 (2018).
5. D. E. Oorschot, Total number of neurons in the neostriatal, pallidal, subthalamic, and substantia nigral nuclei of the rat basal ganglia: A stereological study using the cavalieri and optical disector methods. *J. Comp. Neurol.* **366**, 580–599 (1996).
6. D. A. Burke, H. G. Rotstein, V. A. Alvarez, Striatal local circuitry: A new framework for lateral inhibition. *Neuron* **96**, 267–284 (2017).
7. M. Assous, J. M. Tepper, Excitatory extrinsic afferents to striatal interneurons and interactions with striatal microcircuitry. *Eur. J. Neurosci.* **49**, 593–603 (2019).
8. J. M. Tepper, F. Tecuapetla, T. Koós, O. Ibáñez-Sandoval, Heterogeneity and diversity of striatal GABAergic interneurons. *Front. Neuroanat.* **4**, 150 (2010).
9. C. R. Gerfen, D. J. Surmeier, Modulation of striatal projection systems by dopamine. *Annu. Rev. Neurosci.* **34**, 441–466 (2011).
10. J. Bahuguna, A. Aertsen, A. Kumar, Existence and control of Go/No-Go decision transition threshold in the striatum. *PLoS Comput. Biol.* **11**, e1004233 (2015).
11. K. N. Gurney, M. D. Humphries, P. Redgrave, A new framework for cortico-striatal plasticity: Behavioural theory meets in vitro data at the reinforcement-action interface. *PLoS Biol.* **13**, e1002034 (2015).
12. M. D. Humphries, J. A. Obeso, J. K. Dreyer, Insights into Parkinson's disease from computational models of the basal ganglia. *J. Neurol. Neurosurg. Psychiatry* **89**, 1181–1188 (2018).
13. M. Lindahl, J. Hellgren Kotaleski, Untangling basal ganglia network dynamics and function: Role of dopamine depletion and inhibition investigated in a spiking network model. *eNeuro* **3**, ENEURO.0156-16.2016 (2017).
14. S. M. Suryanarayana, J. Hellgren Kotaleski, S. Grillner, K. N. Gurney, Roles for globus pallidus externa revealed in a computational model of action selection in the basal ganglia. *Neural Netw.* **109**, 113–136 (2019).
15. T. J. Prescott, F. M. Montes González, K. Gurney, M. D. Humphries, P. Redgrave, A robot model of the basal ganglia: Behavior and intrinsic processing. *Neural Netw.* **19**, 31–61 (2006).
16. S. Damodaran, J. R. Cressman, Z. Jedrzejewski-Szmek, K. T. Blackwell, Desynchronization of fast-spiking interneurons reduces β-band oscillations and imbalance in firing in the dopamine-depleted striatum. *J. Neurosci.* **35**, 1149–1159 (2015).
17. S. Damodaran, R. C. Evans, K. T. Blackwell, Synchronized firing of fast-spiking interneurons is critical to maintain balanced firing between direct and indirect pathway neurons of the striatum. *J. Neurophysiol.* **111**, 836–848 (2014).
18. K. Du *et al.*, Cell-type-specific inhibition of the dendritic plateau potential in striatal spiny projection neurons. *Proc. Natl. Acad. Sci. U.S.A.* **114**, E7612–E7621 (2017).
19. R. C. Evans, Y. M. Maniar, K. T. Blackwell, Dynamic modulation of spike timing-dependent calcium influx during corticostriatal upstates. *J. Neurophysiol.* **110**, 1631–1645 (2013).
20. R. C. Evans *et al.*, The effects of NMDA subunit composition on calcium influx and spike timing-dependent plasticity in striatal medium spiny neurons. *PLoS Comput. Biol.* **8**, e1002493 (2012).
21. J. Hjorth, K. T. Blackwell, J. H. Kotaleski, Gap junctions between striatal fast-spiking interneurons regulate spiking activity and synchronization as a function of cortical activity. *J. Neurosci.* **29**, 5276–5286 (2009).
22. J. H. Kotaleski, D. Plenz, K. T. Blackwell, Using potassium currents to solve signal-to-noise problems in inhibitory feedforward networks of the striatum. *J. Neurophysiol.* **95**, 331–341 (2006).
23. J. T. Moyer, J. A. Wolf, L. H. Finkel, Effects of dopaminergic modulation on the integrative properties of the ventral striatal medium spiny neuron. *J. Neurophysiol.* **98**, 3731–3748 (2007).
24. J. A. Wolf *et al.*, NMDA/AMPA ratio impacts state transitions and entrainment to oscillations in a computational model of the nucleus accumbens medium spiny projection neuron. *J. Neurosci.* **25**, 9080–9095 (2005).
25. J. R. Edgerton, J. E. Hanson, C. Günay, D. Jaeger, Dendritic sodium channels regulate network integration in globus pallidus neurons: A modeling study. *J. Neurosci.* **30**, 15146–15159 (2010).
26. K. T. Blackwell *et al.*, Molecular mechanisms underlying striatal synaptic plasticity: Relevance to chronic alcohol consumption and seeking. *Eur. J. Neurosci.* **49**, 768–783 (2019).
27. J. H. Kotaleski, K. T. Blackwell, Modelling the molecular mechanisms of synaptic plasticity using systems biology approaches. *Nat. Rev. Neurosci.* **11**, 239–251 (2010).
28. A. G. Nair, U. S. Bhalla, J. Hellgren Kotaleski, Role of DARPP-32 and ARPP-21 in the emergence of temporal constraints on striatal calcium and dopamine integration. *PLoS Comput. Biol.* **12**, e1005080 (2016).
29. A. G. Nair, O. Gutierrez-Arenas, O. Eriksson, P. Vincent, J. Hellgren Kotaleski, Sensing positive versus negative reward signals through adenylyl cyclase-coupled GPCRs in direct and indirect pathway striatal medium spiny neurons. *J. Neurosci.* **35**, 14017–14030 (2015).
30. M. Hawrylycz *et al.*; MindScope, Inferring cortical function in the mouse visual system through large-scale systems neuroscience. *Proc. Natl. Acad. Sci. U.S.A.* **113**, 7337–7344 (2016).
31. H. Markram *et al.*, Reconstruction and simulation of neocortical microcircuitry. *Cell* **163**, 456–492 (2015).
32. J. R. Crittenden, A. M. Graybiel, Basal Ganglia disorders associated with imbalances in the striatal striosome and matrix compartments. *Front. Neuroanat.* **5**, 59 (2011).
33. A. M. Graybiel, C. W. Ragsdale, Jr, Histochemically distinct compartments in the striatum of human, monkeys, and cat demonstrated by acetylthiocholinesterase staining. *Proc. Natl. Acad. Sci. U.S.A.* **75**, 5723–5726 (1978).
34. J. G. Johnston, C. R. Gerfen, S. N. Haber, D. van der Kooy, Mechanisms of striatal pattern formation: Conservation of mammalian compartmentalization. *Brain Res. Dev. Brain Res.* **57**, 93–102 (1990).
35. M. Stephenson-Jones, A. A. Kardamakis, B. Robertson, S. Grillner, Independent circuits in the basal ganglia for the evaluation and selection of actions. *Proc. Natl. Acad. Sci. U.S.A.* **110**, E3670–E3679 (2013).
36. M. Stephenson-Jones *et al.*, A basal ganglia circuit for evaluating action outcomes. *Nature* **539**, 289–293 (2016).
37. D. J. Surmeier, S. M. Graves, W. Shen, Dopaminergic modulation of striatal networks in health and Parkinson's disease. *Curr. Opin. Neurobiol.* **29**, 109–117 (2014).
38. T. Fieblinger *et al.*, Cell type-specific plasticity of striatal projection neurons in parkinsonism and L-DOPA-induced dyskinesia. *Nat. Commun.* **5**, 5316 (2014).
39. T. S. Gertler, C. S. Chan, D. J. Surmeier, Dichotomous anatomical properties of adult striatal medium spiny neurons. *J. Neurosci.* **28**, 10814–10824 (2008).
40. L. M. Suárez *et al.*, L-DOPA treatment selectively restores spine density in dopamine receptor D2-expressing projection neurons in dyskinetic mice. *Biol. Psychiatry* **75**, 711–722 (2014).
41. M. Day, D. Wokosin, J. L. Plotkin, X. Tian, D. J. Surmeier, Differential excitability and modulation of striatal medium spiny neuron dendrites. *J. Neurosci.* **28**, 11603–11614 (2008).
42. H. Planert, T. K. Berger, G. Silberberg, Membrane properties of striatal direct and indirect pathway neurons in mouse and rat slices and their modulation by dopamine. *PLoS One* **8**, e57054 (2013).
43. H. Planert, S. N. Szydlowski, J. J. Hjorth, S. Grillner, G. Silberberg, Dynamics of synaptic transmission between fast-spiking interneurons and striatal projection neurons of the direct and indirect pathways. *J. Neurosci.* **30**, 3499–3507 (2010).
44. S. N. Szydlowski *et al.*, Target selectivity of feedforward inhibition by striatal fast-spiking interneurons. *J. Neurosci.* **33**, 1678–1683 (2013).
45. T. Koós, J. M. Tepper, Inhibitory control of neostriatal projection neurons by GABAergic interneurons. *Nat. Neurosci.* **2**, 467–472 (1999).
46. G. Russo, T. R. Nieus, S. Maggi, S. Taverna, Dynamics of action potential firing in electrically connected striatal fast-spiking interneurons. *Front. Cell. Neurosci.* **7**, 209 (2013).
47. J. M. Tepper *et al.*, Heterogeneity and diversity of striatal GABAergic interneurons: Update 2018. *Front. Neuroanat.* **12**, 91 (2018).
48. Y. Kawaguchi, Large aspiny cells in the matrix of the rat neostriatum in vitro: Physiological identification, relation to the compartments and excitatory postsynaptic currents. *J. Neurophysiol.* **67**, 1669–1682 (1992).
49. S. Threlfell *et al.*, Striatal dopamine release is triggered by synchronized activity in cholinergic interneurons. *Neuron* **75**, 58–64 (2012).
50. R. Reig, G. Silberberg, Multisensory integration in the mouse striatum. *Neuron* **83**, 1200–1212 (2014).
51. J. N. Reynolds, B. I. Hyland, J. R. Wickens, Modulation of an afterhyperpolarization by the substantia nigra induces pauses in the tonic firing of striatal cholinergic interneurons. *J. Neurosci.* **24**, 9870–9877 (2004).
52. C. J. Wilson, The mechanism of intrinsic amplification of hyperpolarizations and spontaneous bursting in striatal cholinergic interneurons. *Neuron* **45**, 575–585 (2005).
53. M. E. Anderson, Discharge patterns of basal ganglia neurons during active maintenance of postural stability and adjustment to chair tilt. *Brain Res.* **143**, 325–338 (1978).
54. T. Aosaki *et al.*, Responses of tonically active neurons in the primate's striatum undergo systematic changes during behavioral sensorimotor conditioning. *J. Neurosci.* **14**, 3969–3984 (1994).

55. M. Kimura, J. Rajkowski, E. Evarts, Tonically discharging putamen neurons exhibit set-dependent responses. *Proc. Natl. Acad. Sci. U.S.A.* **81**, 4998–5001 (1984).
56. P. Apicella, E. Legallet, E. Trouche, Responses of tonically discharging neurons in the monkey striatum to primary rewards delivered during different behavioral states. *Exp. Brain Res.* **116**, 456–466 (1997).
57. C. D. Fiorillo, P. N. Tobler, W. Schultz, Discrete coding of reward probability and uncertainty by dopamine neurons. *Science* **299**, 1898–1902 (2003).
58. G. Morris, D. Arkadir, A. Nevet, E. Vaadia, H. Bergman, Coincident but distinct messages of midbrain dopamine and striatal tonically active neurons. *Neuron* **43**, 133–143 (2004).
59. B. D. Bennett, J. C. Callaway, C. J. Wilson, Intrinsic membrane properties underlying spontaneous tonic firing in neostriatal cholinergic interneurons. *J. Neurosci.* **20**, 8493–8503 (2000).
60. M. J. Oswald, D. E. Oorschot, J. M. Schulz, J. Lipski, J. N. Reynolds, IH current generates the afterhyperpolarisation following activation of subthreshold cortical synaptic inputs to striatal cholinergic interneurons. *J. Physiol.* **587**, 5879–5897 (2009).
61. E. Fino, M. Vandecasteele, S. Perez, F. Saudou, L. Venance, Region-specific and state-dependent action of striatal GABAergic interneurons. *Nat. Commun.* **9**, 3339 (2018).
62. K. C. Luk, A. F. Sadikot, GABA promotes survival but not proliferation of parvalbumin-immunoreactive interneurons in rodent neostriatum: An in vivo study with stereology. *Neuroscience* **104**, 93–103 (2001).
63. M. Matamales, J. Götz, J. Bertran-Gonzalez, Quantitative imaging of cholinergic interneurons reveals a distinctive spatial organization and a functional gradient across the mouse striatum. *PLoS One* **11**, e0157682 (2016).
64. Y. Nakano *et al*., Parvalbumin-producing striatal interneurons receive excitatory inputs onto proximal dendrites from the motor thalamus in male mice. *J. Neurosci. Res.* **96**, 1186–1207 (2018).
65. K. Ren *et al*., Striatal distribution and cytoarchitecture of dopamine receptor subtype 1 and 2: Evidence from double-labeling transgenic mice. *Front. Neural Circuits* **11**, 57 (2017).
66. H. Hintiryan *et al*., The mouse cortico-striatal projectome. *Nat. Neurosci.* **19**, 1100–1114 (2016).
67. B. M. Hooks *et al*., Author Correction: Topographic precision in sensory and motor corticostriatal projections varies across cell type and cortical area. *Nat. Commun.* **9**, 4317 (2018).
68. B. J. Hunnicutt *et al*., A comprehensive excitatory input map of the striatum reveals novel functional organization. *eLife* **5**, e19103 (2016).
69. G. Mandelbaum *et al*., Distinct cortical-thalamic-striatal circuits through the parafascicular nucleus. *Neuron* **102**, 636–652.e7 (2019).
70. G. Gangarossa *et al*., Spatial distribution of D1R- and D2R-expressing medium-sized spiny neurons differs along the rostro-caudal axis of the mouse dorsal striatum. *Front. Neural Circuits* **7**, 124 (2013).
71. A. Märtin *et al*., A spatiomolecular map of the striatum. *Cell Rep.* **29**, 4320–4333.e5 (2019).
72. Y. Miyamoto, S. Katayama, N. Shigematsu, A. Nishi, T. Fukuda, Striosome-based map of the mouse striatum that is conformable to both cortical afferent topography and uneven distributions of dopamine D1 and D2 receptor-expressing cells. *Brain Struct. Funct.* **223**, 4275–4291 (2018).
73. Y. Miyamoto, I. Nagayoshi, A. Nishi, T. Fukuda, Three divisions of the mouse caudal striatum differ in the proportions of dopamine D1 and D2 receptor-expressing cells, distribution of dopaminergic axons, and composition of cholinergic and GABAergic interneurons. *Brain Struct. Funct.* **224**, 2703–2716 (2019).
74. G. Stanley, O. Gokce, R. C. Malenka, T. C. Südhof, S. R. Quake, Discrete and continuous cell identities of the adult murine striatum. bioRxiv:591396 (27 March 2019).
75. G. D. Rosen, R. W. Williams, Complex trait analysis of the mouse striatum: Independent QTLs modulate volume and neuron number. *BMC Neurosci.* **2**, 5 (2001).
76. G. A. Graveland, M. DiFiglia, The frequency and distribution of medium-sized neurons with indented nuclei in the primate and rodent neostriatum. *Brain Res.* **327**, 307–311 (1985).
77. J. M. Tepper, T. Koós, C. J. Wilson, GABAergic microcircuits in the neostriatum. *Trends Neurosci.* **27**, 662–669 (2004).
78. M. I. Ransome, A. M. Turnley, Analysis of neuronal subpopulations in mice overexpressing suppressor of cytokine signaling-2. *Neuroscience* **132**, 673–687 (2005).
79. O. Ibáñez-Sandoval *et al*., A novel functionally distinct subtype of striatal neuropeptide Y interneuron. *J. Neurosci.* **31**, 16757–16769 (2011).
80. H. Janickova, V. F. Prado, M. A. M. Prado, S. El Mestikawy, V. Bernard, Vesicular acetylcholine transporter (VAChT) over-expression induces major modifications of striatal cholinergic interneuron morphology and function. *J. Neurochem.* **142**, 857–875 (2017).
81. S. Taverna, E. Ilijic, D. J. Surmeier, Recurrent collateral connections of striatal medium spiny neurons are disrupted in models of Parkinson's disease. *J. Neurosci.* **28**, 5504–5512 (2008).
82. M. J. Tunstall, D. E. Oorschot, A. Kean, J. R. Wickens, Inhibitory interactions between spiny projection neurons in the rat striatum. *J. Neurophysiol.* **88**, 1263–1269 (2002).
83. F. N. Garas *et al*., Secretagogin expression delineates functionally-specialized populations of striatal parvalbumin-containing interneurons. *eLife* **5**, e16088 (2016).
84. H. Kita, T. Kosaka, C. W. Heizmann, Parvalbumin-immunoreactive neurons in the rat neostriatum: A light and electron microscopic study. *Brain Res.* **536**, 1–15 (1990).
85. Y. Kubota, Y. Kawaguchi, Dependence of GABAergic synaptic areas on the interneuron type and target size. *J. Neurosci.* **20**, 375–386 (2000).
86. C. Aoki, V. M. Pickel, Neuropeptide Y-containing neurons in the rat striatum: Ultrastructure and cellular relations with tyrosine hydroxylase- containing terminals and with astrocytes. *Brain Res.* **459**, 205–225 (1988).
87. M. DiFiglia, N. Aronin, Ultrastructural features of immunoreactive somatostatin neurons in the rat caudate nucleus. *J. Neurosci.* **2**, 1267–1274 (1982).
88. J. Vuillet, L. Kerkerian, P. Kachidian, O. Bosler, A. Nieoullon, Ultrastructural correlates of functional relationships between nigral dopaminergic or cortical afferent fibers and neuropeptide Y-containing neurons in the rat striatum. *Neurosci. Lett.* **100**, 99–104 (1989).
89. J. Vuillet, L. Kerkerian, P. Salin, A. Nieoullon, Ultrastructural features of NPY-containing neurons in the rat striatum. *Brain Res.* **477**, 241–251 (1989).
90. C. Straub *et al*., Principles of synaptic organization of GABAergic interneurons in the striatum. *Neuron* **92**, 84–92 (2016).
91. R. Elghaba, N. Vautrelle, E. Bracci, Mutual control of cholinergic and low-threshold spike interneurons in the striatum. *Front. Cell. Neurosci.* **10**, 111 (2016).
92. A. E. Melendez-Zaidi, H. Lakshminarasimhah, D. J. Surmeier, Cholinergic modulation of striatal nitric oxide-producing interneurons. *Eur. J. Neurosci.* **50**, 3713–3731 (2019).
93. V. Bernard, E. Normand, B. Bloch, Phenotypical characterization of the rat striatal neurons expressing muscarinic receptor genes. *J. Neurosci.* **12**, 3591–3600 (1992).
94. T. Koós, J. M. Tepper, Dual cholinergic control of fast-spiking interneurons in the neostriatum. *J. Neurosci.* **22**, 529–535 (2002).
95. D. F. English *et al*., GABAergic circuits mediate the reinforcement-related signals of striatal cholinergic interneurons. *Nat. Neurosci.* **15**, 123–130 (2011).
96. M. Assous *et al*., Differential processing of thalamic information via distinct striatal interneuron circuits. *Nat. Commun.* **8**, 15860 (2017).
97. A. B. Munoz-Manchado *et al*., Diversity of interneurons in the dorsal striatum revealed by single-cell RNA sequencing and PatchSeq. *Cell Rep.* **24**, 2179–2190.e7 (2018).
98. T. Koos, J. M. Tepper, C. J. Wilson, Comparison of IPSCs evoked by spiny and fast-spiking neurons in the neostriatum. *J. Neurosci.* **24**, 7916–7922 (2004).
99. A. A. Mamaligas, C. P. Ford, Spontaneous synaptic activation of muscarinic receptors by striatal cholinergic neuron firing. *Neuron* **91**, 574–586 (2016).
100. Y. Johansson, G. Silberberg, The functional organization of cortical and thalamic inputs onto five types of striatal neurons is determined by source and target cell identities. *Cell Rep.* **30**, 1178–1194.e3 (2020).
101. J. L. Plotkin, M. Day, D. J. Surmeier, Synaptically driven state transitions in distal dendrites of striatal spiny neurons. *Nat. Neurosci.* **14**, 881–888 (2011).
102. S. Nonomura *et al*., Monitoring and updating of action selection for goal-directed behavior through the striatal direct and indirect pathways. *Neuron* **99**, 1302–1314.e5 (2018).
103. J. G. Parker *et al*., Diametric neural ensemble dynamics in parkinsonian and dyskinetic states. *Nature* **557**, 177–182 (2018).
104. M. Assous, D. Dautan, J. M. Tepper, J. Mena-Segovia, Pedunculopontine glutamatergic neurons provide a novel source of feedforward inhibition in the striatum by selectively targeting interneurons. *J. Neurosci.* **39**, 4727–4737 (2019).
105. M. A. Sullivan, H. Chen, H. Morikawa, Recurrent inhibitory network among striatal cholinergic interneurons. *J. Neurosci.* **28**, 8682–8690 (2008).
106. R. Lindroos *et al*., Basal ganglia neuromodulation over multiple temporal and structural scales-simulations of direct pathway MSNs investigate the fast onset of dopaminergic effects and predict the role of Kv4.2. *Front. Neural Circuits* **12**, 3 (2018).
107. S. Casali, E. Marenzi, C. Medini, C. Casellato, E. D'Angelo, Corrigendum: Reconstruction and simulation of a scaffold model of the cerebellar network. *Front. Neuroinform.* **13**, 51 (2019).
108. R. Migliore *et al*., The physiological variability of channel density in hippocampal CA1 pyramidal cells and interneurons explored using a unified data-driven modeling workflow. *PLoS Comput. Biol.* **14**, e1006423 (2018).
109. K. Dai *et al*., The SONATA data format for efficient description of large-scale network models. bioRxiv:625491 (20 September 2019).
110. P. Deng, Y. Zhang, Z. C. Xu, Involvement of I(h) in dopamine modulation of tonic firing in striatal cholinergic interneurons. *J. Neurosci.* **27**, 3148–3156 (2007).
111. E. B. Wilson, Probable interference, the law of succession, and statistical interference. *J. Am. Stat. Assoc.* **22**, 209–212 (1927).
112. A. H. Gittis, A. B. Nelson, M. T. Thwin, J. J. Palop, A. C. Kreitzer, Distinct roles of GABAergic interneurons in the regulation of striatal output pathways. *J. Neurosci.* **30**, 2223–2234 (2010).